V International Conference on Simulation for Additive Manufacturing
Sim-AM 2025
F. Auricchio, M. Carraturo and S. Morganti (Eds)

A THERMAL-HISTORY-INFORMED INHERENT STRAIN FRAMEWORK FOR EFFICIENT DISTORTION PREDICTION IN PBF-LB

I. Setien[*], Michele Chiumenti[††] and Maria San Sebastian[*]**

[*] LORTEK, Basque Research and Technology Alliance (BRTA),
Arranomendia Kalea 4A, Ordizia, 20240, Spain

[**] International Center for Numerical Methods in Engineering (CIMNE),
Edificio C1, Campus Norte, Gran Capitán s/n, Barcelona, 08034, Spain

[††] Technical University of Catalonia,
Edificio C1, Campus Norte, Gran Capitán s/n, Barcelona, 08034, Spain

Key words: Laser Powder Bed Fusion (LPBF), Inherent Strain Method (ISM), Geometry-aware lumping, Distortion prediction, Ti-6Al-4V.

Abstract. This work advances a temperature-history-informed inherent strain framework (Enhanced Inherent Strain Method (EISM)) for efficient, part-scale distortion prediction in metal Powder Bed Fusion - Laser Beam (PBF-LB). A layer-wise, energy-equivalent thermal analysis supplies an averaged temperature history used to modulate the applied inherent strain tensor. To address accuracy losses near structural transitions (shrink-line-prone regions), two geometry-aware lumping strategies are introduced: local mesh refinement and partial element activation within a confined height window. The study focuses on a Bridge benchmark in Ti–6Al–4V, reusing previously published experimental datasets for validation. Results show that, relative to classical Inherent Strain Method (ISM), EISM improves the magnitude and shape of as-built deflections; moreover, geometry-aware lump reduction recovers most of the accuracy of fine uniform lumping at a fraction of its cost. Post-cut top-surface deflection is captured robustly across cases when the baseline inherent strain is consistent with the process. Practical guidance is provided on selecting lump sizes and when to deploy local reduction.

1 INTRODUCTION

Metal PBF-LB enables the fabrication of lightweight, topology-optimised components aligned with Industry 4.0 and sustainability objectives, offering material efficiency and recyclability advantages that have accelerated adoption across aerospace, automotive and healthcare sectors [1], [2]. Despite this promise, rapid thermal cycles, steep temperature gradients and phase changes inherent to the layer-wise process generate residual stresses and distortions that compromise dimensional accuracy and reliability [3].

Physics-based simulation has therefore become central to process understanding and parameter selection. Among available approaches, the classical ISM, adapted from computational welding mechanics [4], delivers practical predictions of part-scale distortion by applying precomputed inherent strains during layer activation and has seen wide uptake in PBF-LB modelling and software tooling [5], [6], [7], [8]. However, the commonly used form of ISM assumes a uniform thermal history and

instantaneous application of the inherent strain upon layer (or lump) activation. In addition, layer-level ISM based methodologies are sensitive to mesh and lumping choices, limiting performance near geometric transitions where strong thermal gradients occur [9]. Recent refinements incorporate temperature-history effects or process-informed inherent strains [10], [11], [12], yet further work is needed to retain efficiency while capturing local, geometry-dependent behaviour.

Within this context, shrink lines (localised surface notches that emerge due to structural transitions in the building direction) are a recurrent defect that degrades dimensional accuracy and may impact fatigue. Recent studies proposed automated, geometry-driven detection of shrink-line-prone transitions and finite-element-based prediction workflows linking overheating to shrink-line depth, demonstrating measurable dimensional improvements on academic and industrial parts [13], [14]. These results motivate modelling strategies that remain computationally efficient while being sensitive to local temperature history and structural transitions.

Building on the previously developed temperature-history-informed ISM framework [15], this article consolidates and advances an EISM in which the applied inherent strains evolve with the simulated thermal history and temperature-dependent material properties. The study introduces two geometry-aware modelling strategies (localised mesh refinement at transition regions and partial element activation) to reduce lumping effects and improve the prediction of shrink-line defects. Accuracy–cost trade-offs and mesh/lumping sensitivities were quantified on a benchmark Bridge case and the approach was further demonstrated on an industrial-scale Steady Blowing Actuator (SBA), achieving enhanced localisation of shrink-line defects. However, to meet space constraints and avoid repeating already published experimental details, the assessment in this paper is limited to the Bridge case.

The remainder of the paper is structured as follows: Section 2 presents the EISM methodology and geometry-aware lumping strategies; Section 3 summarises the experimental context required for interpretability, with full procedures detailed in prior work; Section 4 describes the numerical study design; Section 4 defines the numerical study; Section 5 integrates results and discussion on thermal evolution, deflection in the as-built state and after partial cut, and accuracy–cost trade-offs; finally, Section 6 outlines practical guidance and limitations.

2 EISM METHODOLOGY

The Enhanced Inherent Strain Method (EISM) is a sequentially coupled thermo-mechanical analysis at part scale. A part-scale, layer-wise thermal model provides an averaged temperature history that is then used to adjust the applied inherent strain during the mechanical analysis. The methodology preserves the computational efficiency of classical ISM while introducing temperature dependence and geometry-aware control of layer lumping to improve predictions near stiffness transitions in the build direction (shrink-line-prone regions). A schematic of the data flow is shown in Figure 1.

2.1 Macro-scale thermal analysis

The layer-by-layer macro-scale thermal model follows established part-scale approaches [16]. It is used to calculate the *average* temperature-field evolution of the printed domain immediately before the subsequent (lumped) layer is deposited.

Instead of resolving the moving heat source explicitly, a gradual-heating (equivalent heat input) strategy is applied over each lumped layer (see Figure 2). Therefore, a time-averaged volumetric heat source is applied on each lumped layer during an equivalent time step so that the total absorbed energy

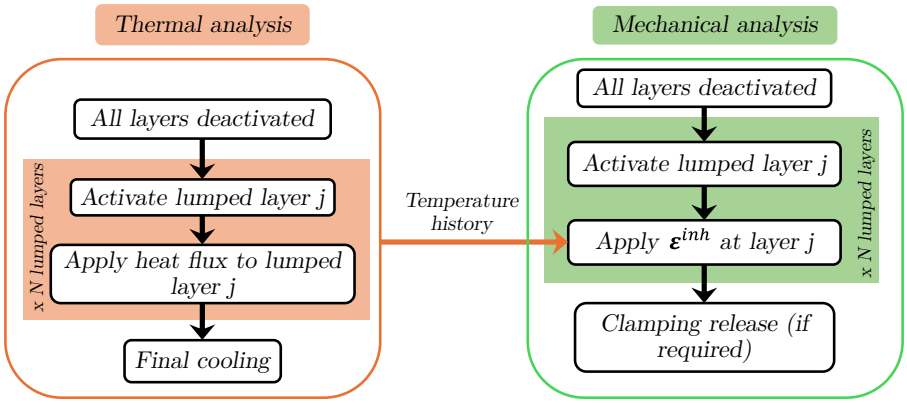

Figure 1: Schematic of the EISM methodology: part-scale thermal history updates the inherent strain in the mechanical analysis.

matches the real process:

$$\dot{Q}_{lumped\_layer} = \frac{\sum_{i=1}^{n} \left(\dot{Q}_i \cdot t_i^{\text{laser}} \right)}{\sum_{i=1}^{n} \left(t_i^{\text{laser}} + t_i^{\text{recoater}} \right)} \quad , \tag{1}$$

where i is the layer index, n denotes the number of layers in each lump, and t_i^{laser} and t_i^{recoater} represent the laser exposure and recoating times for layer i, respectively.

The equivalent time increment for the lumped layer is

$$\Delta t_{lumpend\_layer} = \sum_{i=1}^{n} \left(t_i^{\text{laser}} + t_i^{\text{recoater}} \right) \quad . \tag{2}$$

This construction preserves energy and keeps the total simulated build time unchanged while avoiding path-level resolution at part scale.

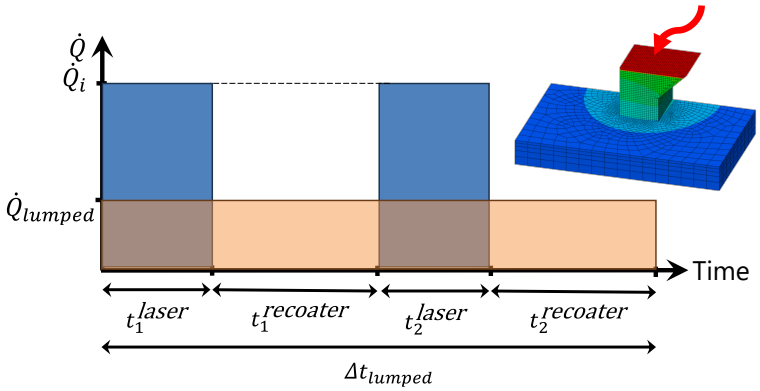

Figure 2: Equivalent heat-input concept for a lumped layer: energy from the measured laser-on intervals within the lump is averaged over the full lump time (laser exposure + recoating).

2.2 Mechanical analysis with temperature-informed inherent strain

The mechanical problem is solved assuming small strain kinematics with a linear elastic constitutive model:

$$\nabla \cdot \boldsymbol{\sigma} = \mathbf{0} \quad , \tag{3}$$

$$\boldsymbol{\sigma} = \boldsymbol{C} : \boldsymbol{\varepsilon}^{e} \quad , \tag{4}$$

$$\boldsymbol{\varepsilon}^{e} = \boldsymbol{\varepsilon}^{\text{tot}} - \boldsymbol{\varepsilon}^{\text{inh}} \quad . \tag{5}$$

The inherent strain $\boldsymbol{\varepsilon}^{\text{inh}}$ collects all non-elastic contributions and is introduced as an eigenstrain. A precomputed tensor $\boldsymbol{\varepsilon}^{\text{inh},0}$ (from experimental calibration [6] or meso-scale simulation [15]) is adopted as baseline. In classical ISM, $\boldsymbol{\varepsilon}^{\text{inh}} = \boldsymbol{\varepsilon}^{\text{inh},0}$ is applied upon activation, independent of T. In EISM, the applied inherent strain is enhanced by a temperature-history term derived from the macro-scale thermal solution:

$$\boldsymbol{\varepsilon}^{\text{inh}}(\mathbf{x}, t) = \boldsymbol{\varepsilon}^{\text{inh},0} + \Delta\boldsymbol{\varepsilon}^{\text{th}}(\mathbf{x}, t), \tag{6}$$

$$\Delta\boldsymbol{\varepsilon}^{\text{th}}(\boldsymbol{x}, t) = \left[\alpha\big(T(\boldsymbol{x}, t)\big)\,(T(\boldsymbol{x}, t) - T_{ref})\right]\boldsymbol{I}, \tag{7}$$

where $\alpha(T)$ is the secant coefficient of thermal expansion and T_{ref} the reference temperature. The baseline $\boldsymbol{\varepsilon}^{\text{inh},0}$ already embeds full cooling to T_{ref}; the additive term in Equation (7) accounts only for the missing, part-scale thermal deformation during building. As all material points reach T_{ref}, $\Delta\boldsymbol{\varepsilon}^{\text{th}} \to \mathbf{0}$.

Additionally, unlike the ISM, the EISM considers *temperature-dependent material properties*, leading to different thermo-mechanical behaviour as the process progresses.

2.3 Material deposition and evolving domain

Layer activation follows a birth-death element activation strategy in both analyses. In thermal steps, inactive elements sharing nodes with active ones are kept at their initial temperature to avoid spurious gradients. In the mechanical steps, activation strains are applied to ensure stress-free introduction of new elements, preventing artificial residuals at interfaces [17], [18].

2.4 Geometry-aware layer lumping

Layer lumping directly governs the time discretisation through equation (2). The selected lump size must preserve the validity of the inherent strain assumption [15] while minimising discretisation errors along the build direction. In addition, the mesh resolution should remain consistent with the chosen lump thickness. Structural transitions along the build height—such as cross-section growth or the onset of new features—must be explicitly addressed, as they induce stiffness jumps and are typically associated with shrink-line formation. These regions can be automatically detected through geometry-based analyses [13], [14]. Prediction accuracy near such transitions is highly sensitive to the local lump thickness and reducing the lump size in these areas generally improves the distortion prediction accuracy associated with shrink-line defects. This observation motivates the introduction of a variable lumping strategy, as sketched in Figure 3.

Implementing local reductions in lump size requires the activation of smaller subdomains and the corresponding application of inherent strains. Two practical approaches are proposed. The first consists of local mesh refinement, which mantains at least one through-thickness element across the effective lump within transition regions; this is shown in Figure 3a. The second approach involves partial element activation within a limited height window in order to emulate reduced lumping without increasing the overall element count; this option is depicted in figure 3b. In the latter case, elements are progressively activated following a simple mixture rule:

$$\boldsymbol{\sigma} = V^{f}\boldsymbol{C} : \boldsymbol{\varepsilon}^{e} \quad , \tag{8}$$

where V^{f} denotes the active material volume fraction of the element, and $\boldsymbol{\varepsilon}^{e}$ represents the homogenised elastic strain.

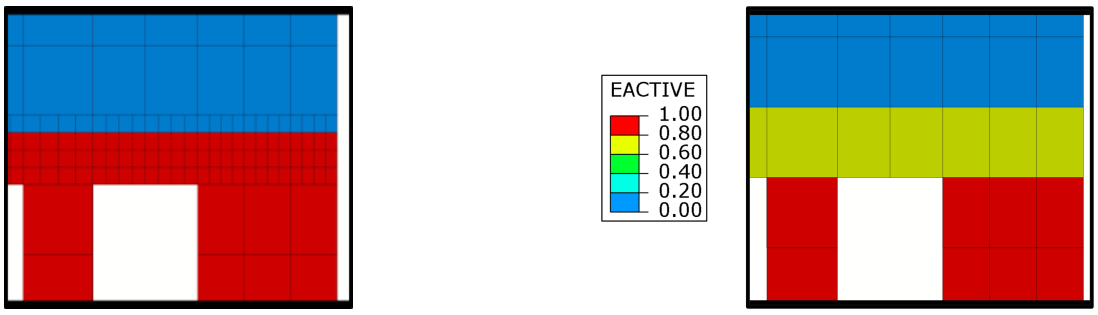

(a) (b)

Figure 3: Geometry-aware variable lumping: (a) local mesh refinement near a stiffness jump, ensuring at least one through-thickness element per effective lump; (b) partial element activation within a limited height window to emulate reduced lumping via a volume-fraction mixture rule.

3 EXPERIMENTAL BASIS AND VALIDATION DATASETS

This section provides the minimum experimental information required to interpret the benchmarks; complete procedures (machine, material, scan strategy, thermocouple installation, path definition and measurement post-processing) are available in [15], [19].

Geometry and setup. A non-symmetric bridge (see Figure 4) in Ti–6Al–4V was fabricated by PBF-LB on an SLM 280 HL-class system. The baseplate was preheated to $200^{\circ}\mathrm{C}$ and the chamber operated at approximately $50^{\circ}\mathrm{C}$, consistent with the modelling assumptions in Section 2. The geometry concentrates stiffness transitions at the supports and at the onset of a top block, known shrink-line-prone regions [13], [14]. CAD, support layout and scan strategy are provided in [15].

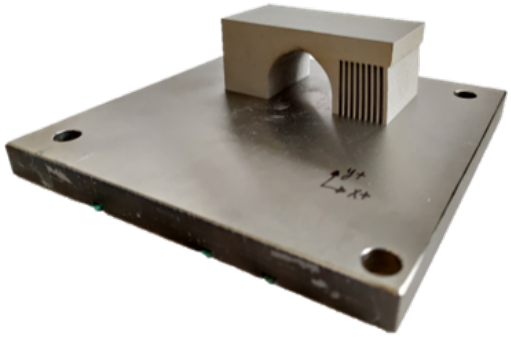

Figure 4: As-built non-symmetric bridge on a $150 \times 150 \times 24\,\mathrm{mm}$ baseplate.

Process timing. Layer-wise laser-on and recoater durations were extracted from machine logs. These measured times were aggregated into lump-equivalent values using Equations (1) and (2) in order to define the energy-equivalent volumetric source and the lump durations used by the macro thermal model.

Temperature traces (baseplate). Six K-type thermocouples were embedded in the baseplate beneath selected locations. The signals were time-aligned to the build timeline and sampled at lump ends to provide slowly varying temperature histories near the part–plate interface. Positions and installation details were documented in [15].

Distortion measurements. Two deflection datasets were acquired on the bridge: (i) *as-built* longitudinal deflection along a front path before any release, and (ii) top-surface deflection along a trans-

verse path after a controlled partial release by wire electrical discharge machining (wEDM). Path definitions, metrology procedures and uncertainty handling are described in [15]. Residual-stress and SBA-related datasets from prior publications were not considered here to meet the page limit.

4 NUMERICAL STUDY DESIGN

This section defines the Bridge-only plan used in Section 5. The detailed thermal and mechanical formulations, material data and calibration procedures are documented in the earlier work and are not repeated here; readers are referred to [15], [19]. Case labels below are reused verbatim in all plots for consistency.

The numerical study in Table 1 was structured to perform a sensitivity analysis and validation on the Bridge geometry. Both ISM and EISM were exercised under different mesh resolutions and lumping strategies. Besides uniform (constant) lumping, two *geometry-aware* schemes that locally reduce lump size in stiffness-transition zones were considered: (i) partial element activation and (ii) local mesh refinement. These cases were selected to quantify accuracy–cost trade-offs.

All cases use Ti–6Al–4V data and the same precomputed $\boldsymbol{\varepsilon}^{\mathrm{inh},0}$ as in [15]. "Lump size" denotes the uniform (base) number of physical layers per lump outside transition regions (cf. Equation (2)). The term "variable" indicates geometry-aware handling confined to the transition window illustrated in Figure 3.

This transition window is centred at the support–to–block onset (a shrink-line-prone zone). In the *partial activation* option (Figure 3b), each 0.96 mm through-thickness element is activated in sub-steps using a volume-fraction rule, e.g. $V^f = \{0.25 \rightarrow 0.50 \rightarrow 1.00\}$, scaling both stiffness and inherent strain with V^f. In the *local mesh refinement* option (Figure 3a), the global 0.96 mm mesh is replaced locally by 4×0.24 mm layers across the transition; activation follows $0.24 \rightarrow 0.24 \rightarrow 0.48$ mm to emulate reduced lumping while limiting increments.

Table 1: Bridge simulation cases (labels match the figures).

#	Case label	Method	Elem. size (mm)	Lumping / Transition handling
01	`ISM_mesh-024_lump-4`	ISM	0.24	Const-4 (uniform)
02	`ISM_mesh-024_lump-16`	ISM	0.24	Const-16 (uniform)
03	`ISM_mesh-096_lump-16`	ISM	0.96	Const-16 (uniform)
04	`EISM_mesh-024_lump-4`	EISM	0.24	Const-4 (uniform)
05	`EISM_mesh-024_lump-16`	EISM	0.24	Const-16 (uniform)
06	`EISM_mesh-096_lump-16`	EISM	0.96	Const-16 (uniform)
07	`ISM_mesh-096_lump-16-variable-partialAct`	ISM	0.96	Const-16 + partial activation
08	`ISM_mesh-096_lump-16-variable-meshRefined`	ISM	0.96	Const-16 + local mesh refinement
09	`EISM_mesh-096_lump-16-variable-partialAct`	EISM	0.96	Const-16 + partial activation
10	`EISM_mesh-096_lump-16-variable-meshRefined`	EISM	0.96	Const-16 + local mesh refinement

5 RESULTS AND DISCUSSION

The analysis concentrates on (i) temperature evolution at the baseplate, (ii) longitudinal deflection in the as-built state along the front path and (iii) top-surface deflection after a controlled partial cut with wEDM. Accuracy is quantified against the experimental curves from prior work and efficiency is measured as total CPU time. Unless stated otherwise, case labels match Table 1.

5.1 Temperature evolution at thermocouple locations

The layer-lumped, part-scale thermal model reproduces the slowly varying temperature level observed by the six baseplate thermocouples for all EISM cases. As an example, in Figure 5 the comparison for thermocouples TC-1 and TC-5 locations are plotted. Differences among numerical cases are small, indicating limited sensitivity to the tested mesh and lumping combinations at the macro scale. Peak values at local hot spots (e.g., near bridging) are modestly higher for smaller lumps, but these differences do not materially alter the subsequent mechanical predictions. As expected for a macro model, high-frequency melt-pool transients are not captured; the averaged thermal history needed by Equation (7) is nevertheless consistent with measurements.

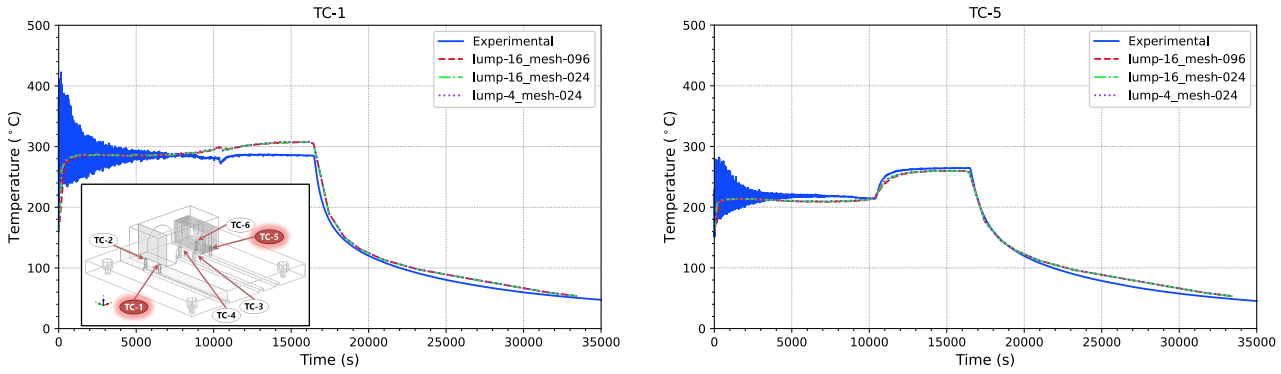

(a) (b)

Figure 5: Comparison between numerically predicted and experimentally recorded temperature histories at thermocouple locations: (a) TC-1 and (b) TC-5.

5.2 As-built longitudinal deflection (front path)

As shown in Figure 6, the front-path deflection exhibits two distinct curvatures: a lower curvature governed by the right support leg and an upper curvature governed by the top block. Uniform-lumping ISM cases (`#01–#03`) systematically underestimate the overall profile. In contrast, uniform-lumping EISM cases improve both magnitude and shape. The fine-lump EISM case (`#04`) provides the closest agreement, capturing the leg curvature and the upper segment with low bias. The coarser uniform EISM options (`#05–#06`) retain the correct upper shape but underpredict the lower curvature, highlighting sensitivity to lump size at stiffness transitions.

To mitigate this local error at the support–to–block onset, geometry-aware variable lumping is applied. The implemented discretisations in the transition window are illustrated in Figure 7, where the u_1 displacement field emphasises how local lump reduction concentrates deformation near the shrink-line-prone interface. In that figure, Case #04 is included as a *fine-lumping reference* against which the variable strategies with coarser global meshes are compared. Both variable EISM strategies

(#09, partial activation, and #10, local mesh refinement) improve the lower-leg curvature relative to their uniform counterpart. When the window is confined as in Figure 3, partial activation (b) avoids adding elements, whereas local mesh refinement (c) reproduces the fine-lump pattern (a) more explicitly.

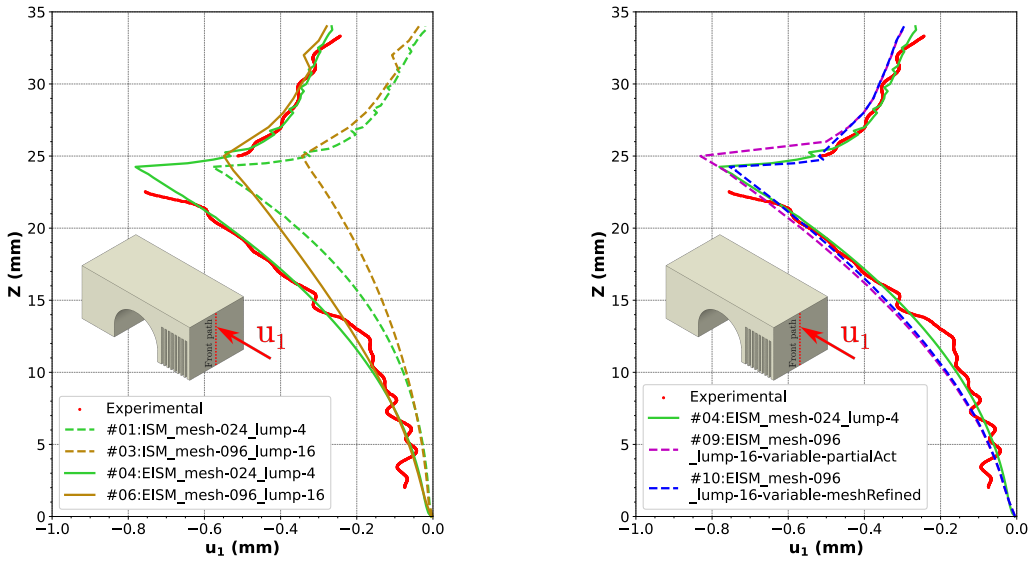

(a) (b)

Figure 6: As-built longitudinal deflection along the front path: experiment vs. simulated cases: (a) methodology and lumping size effect; (b) lumping strategy effect (partial activation / local mesh refinement).

5.3 Top-surface deflection after partial cut

Following the controlled wEDM cut, the top-path deflection is reproduced consistently across all cases (Figure 8). This response predominantly reflects the global residual state at the end of build and cool-down; hence, once the precomputed $\varepsilon^{\mathrm{inh},0}$ is consistent with the material and process, both ISM and EISM capture the shape and magnitude. Variations due to mesh resolution, lump size, or geometry-aware strategies remain within the experimental repeatability band along this path, confirming that the main sensitivity to lumping arises locally at stiffness transitions rather than in the global release measured here.

5.4 Accuracy metrics

Accuracy trends are consistent across the front-path comparisons and are compactly reflected in the cost–accuracy map of Figure 9. Uniform ISM cases (#01–#03) form the upper band with the largest errors (high RMSE). Introducing EISM lowers the error at fixed lumping: the uniform EISM set (#04–#06) shifts downward, with the fine-lump reference #04 attaining the lowest RMSE and removing the underestimation bias. Crucially, the geometry-aware EISM variants at coarse global mesh (#09, #10) recover most of the accuracy gain of #04 while retaining a 0.96 mm base resolution away from the transition. This confirms that the accuracy loss for large uniform lumps is dominated by stiffness jumps and can be mitigated effectively by targeted lump reduction in the transition window.

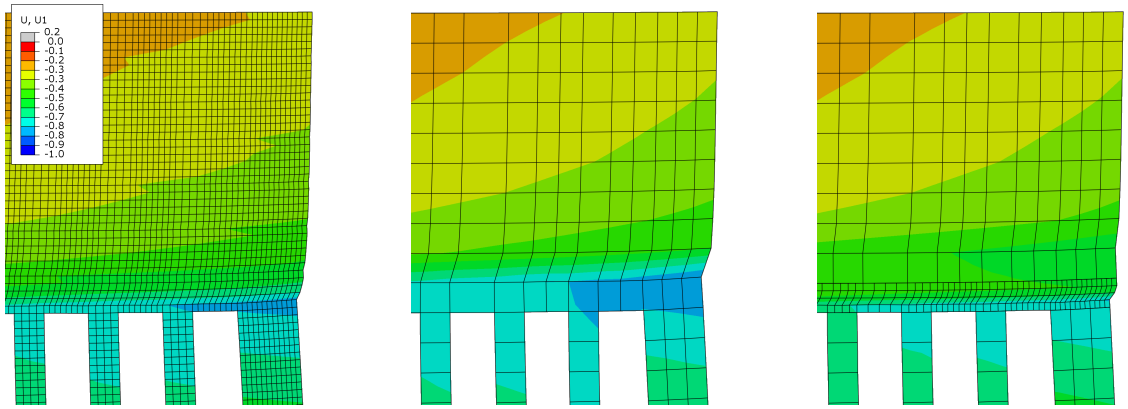

(a) (b) (c)

Figure 7: Zoomed views at the support–to–block transition showing the in-plane displacement field u_1 (contours) over the corresponding discretisation: (a) Case #04 (fine-lumping *reference*), (b) Case #09 (partial activation) and (c) Case #10 (local mesh refinement). Reduced lumping at the transition ((b)–(c)) emulates the local behaviour of the fine-lump case ((a). For comparability, all panels use the same u_1 range and color scale.

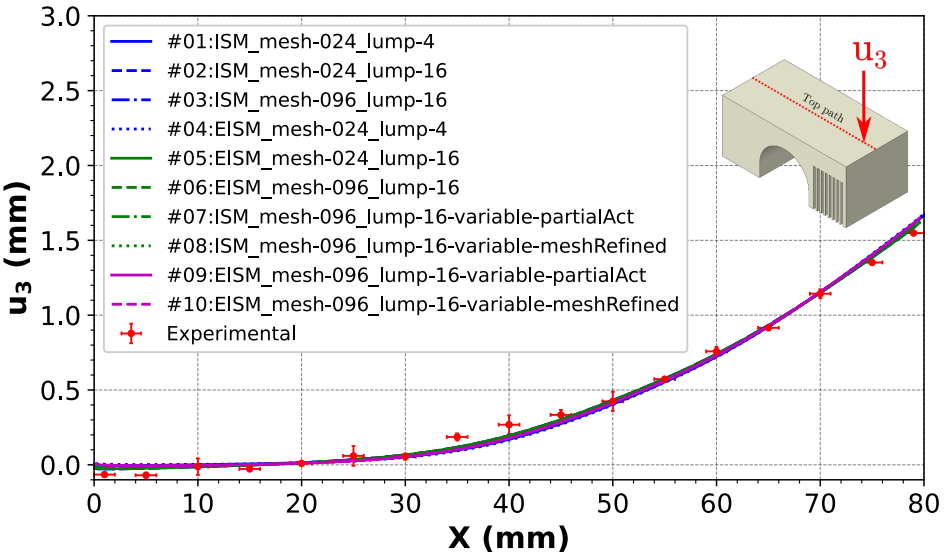

Figure 8: Top-surface deflection along the longitudinal path after partial wEDM cut: experiment versus simulations for cases #01–#10 (labels as in Table 1).

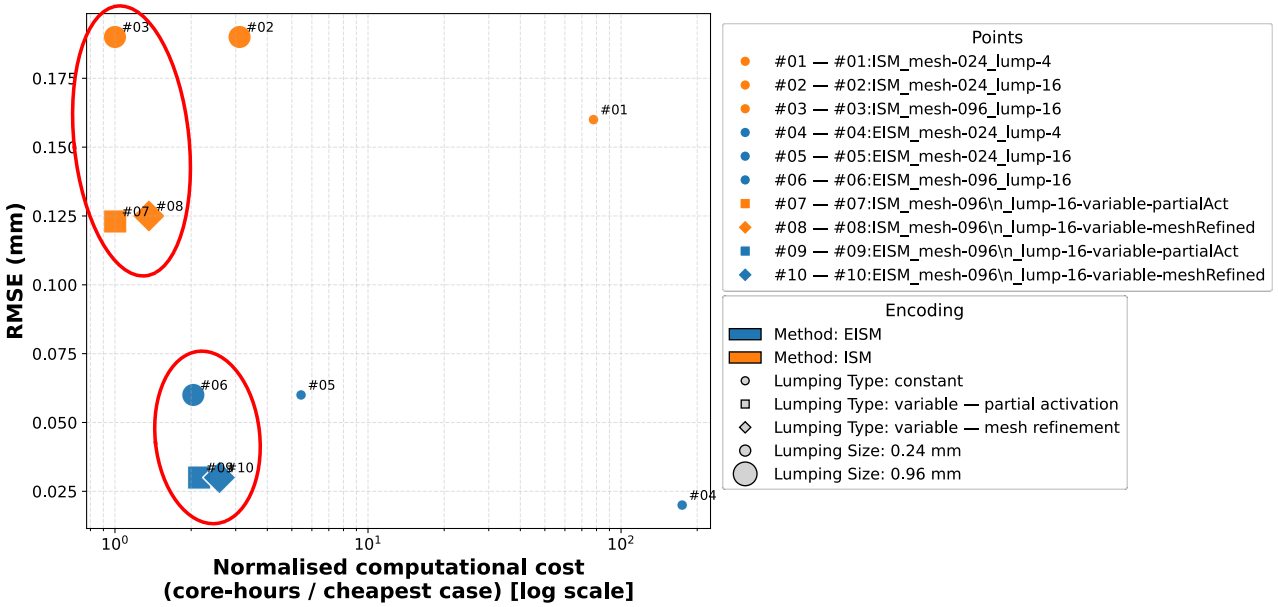

Figure 9: Accuracy–cost trade-off for all Bridge cases: RMSE (front-path deflection) vs. normalised computational cost (core-hours divided by the cheapest case; log scale).

5.5 Computational efficiency

Uniform-lumping comparisons indicate that reducing the lump from 16 to 4 layers increases CPU time strongly, independent of method, due to the larger number of increments. Enabling EISM roughly doubles the cost versus ISM because of the additional thermal analysis. Variable-lumping strategies add only local work: partial activation increases time marginally through extra activation sub-steps, whereas local mesh refinement increases time through additional elements restricted to the transition window. Overall, the `EISM_mesh-096_lump-16-variable-*` family offers a favourable accuracy–cost compromise: near-uniform performance on the top path, improved lower-leg curvature on the front path, and costs closer to coarse uniform runs than to fine uniform runs. This pattern supports adopting geometry-aware lump reduction as a default for shrink-line-prone regions. Figure 9 summarises this trade-off.

6 CONCLUSIONS

A temperature-history-informed inherent strain framework (EISM) was presented for part-scale distortion prediction in PBF-LB. The approach augments a classical ISM with (i) energy-equivalent macro thermal histories and (ii) temperature-dependent material properties, while enabling geometry-aware layer lumping. On the Bridge benchmark, EISM reduces bias in as-built deflection near stiffness transitions and improves agreement after partial release. Computational overhead is moderate when small lumps are confined to transition regions. Recommended practice is to combine EISM with variable lumping triggered by geometry analysis, reserving fine lumping for shrink-line-prone zones. Future work will automate region detection and couple the framework with compensation workflows.

REFERENCES

[1] T. DebRoy, H. Wei, J. Zuback, T. Mukherjee, J. Elmer, J. Milewski, A. Beese, A. Wilson-Heid, A. De, and W. Zhang, “Additive manufacturing of metallic components – process, struc-

ture and properties," *Progress in Materials Science*, vol. 92, no. Supplement C, pp. 112–224, Mar. 2018, ISSN: 0079-6425. DOI: 10.1016/j.pmatsci.2017.10.001. [Online]. Available: http://www.sciencedirect.com/science/article/pii/S0079642517301172.

[2] S. Ford and M. Despeisse, "Additive manufacturing and sustainability: An exploratory study of the advantages and challenges," *Journal of Cleaner Production*, vol. 137, pp. 1573–1587, Nov. 2016, ISSN: 0959-6526. DOI: 10.1016/j.jclepro.2016.04.150.

[3] M. F. Zaeh and G. Branner, "Investigations on residual stresses and deformations in selective laser melting," *Production Engineering*, vol. 4, pp. 35–45, 2010, ISSN: 09446524. DOI: 10.1007/s11740-009-0192-y.

[4] Y. Ueda, H. Murakawa, K. Nakacho, and N. Ma, "Establishment of computational welding mechanics," *Welding and Surfacing Reviews*, vol. 8, no. 1, pp. 265–299, 1997, cited By 4.

[5] N. Keller and V. Ploshikhin, "New method for fast predictions of residual stress and distortion of am parts," 2015. [Online]. Available: https://sffsymposium.engr.utexas.edu/sites/default/files/2014-096-Keller.pdf.

[6] I. Setien, M. Chiumenti, S. van der Veen, M. San Sebastian, F. Garciandía, and A. Echeverría, "Empirical methodology to determine inherent strains in additive manufacturing," *Computers & Mathematics with Applications*, Simulation for Additive Manufacturing, vol. 78, no. 7, pp. 2282–2295, Oct. 2019, ISSN: 0898-1221. DOI: 10.1016/j.camwa.2018.05.015. Accessed: Oct. 24, 2024. [Online]. Available: https://www.sciencedirect.com/science/article/pii/S0898122118302839.

[7] H. Mohammadtaheri, R. Sedaghati, and M. Molavi-Zarandi, "Inherent strain approach to estimate residual stress and deformation in the laser powder bed fusion process for metal additive manufacturing—a state-of-the-art review," en, *The International Journal of Advanced Manufacturing Technology*, vol. 122, no. 5, pp. 2187–2202, Sep. 2022, ISSN: 1433-3015. DOI: 10.1007/s00170-022-10052-2. Accessed: May 18, 2023. [Online]. Available: https://doi.org/10.1007/s00170-022-10052-2.

[8] M. Bayat, W. Dong, J. Thorborg, A. C. To, and J. H. Hattel, "A review of multi-scale and multi-physics simulations of metal additive manufacturing processes with focus on modeling strategies," en, *Additive Manufacturing*, vol. 47, p. 102 278, Nov. 2021, ISSN: 2214-8604. DOI: 10.1016/j.addma.2021.102278. Accessed: Jan. 18, 2023. [Online]. Available: https://www.sciencedirect.com/science/article/pii/S2214860421004383.

[9] M. Bugatti and Q. Semeraro, "Limitations of the inherent strain method in simulating powder bed fusion processes," *Additive Manufacturing*, 2018, ISSN: 2214-8604. DOI: 10.1016/j.addma.2018.05.041. [Online]. Available: http://www.sciencedirect.com/science/article/pii/S2214860417302877.

[10] W. Dong, X. A. Jimenez, and A. C. To, "Temperature-dependent modified inherent strain method for predicting residual stress and distortion of Ti6Al4V walls manufactured by wire-arc directed energy deposition," en, *Additive Manufacturing*, vol. 62, p. 103 386, Jan. 2023, ISSN: 2214-8604. DOI: 10.1016/j.addma.2022.103386. Accessed: Jan. 18, 2023. [Online]. Available: https://www.sciencedirect.com/science/article/pii/S2214860422007758.

[11] T. Du, P. Yan, Q. Liu, and L. Dong, "A process-based inherent strain method for prediction of deformation and residual stress for wire-arc directed energy deposition," en, *Computational Mechanics*, Oct. 2023, ISSN: 1432-0924. DOI: 10.1007/s00466-023-02400-0. Ac-

cessed: Oct. 30, 2023. [Online]. Available: https://doi.org/10.1007/s00466-023-02400-0.

[12] P. Pourabdollah, F. Farhang Mehr, S. Cockcroft, and D. Maijer, "A new variant of the inherent strain method for the prediction of distortion in powder bed fusion additive manufacturing processes," en, *The International Journal of Advanced Manufacturing Technology*, Feb. 2024, ISSN: 1433-3015. DOI: 10.1007/s00170-024-13255-x. Accessed: Mar. 5, 2024. [Online]. Available: https://doi.org/10.1007/s00170-024-13255-x.

[13] D. Rauner, D. Wolf, L. Spano, and M. F. Zaeh, "A method for the predictive and automated detection of the shrink line location during the powder bed fusion of metals using a laser beam," *Procedia CIRP*, 17th CIRP Conference on Intelligent Computation in Manufacturing Engineering (CIRP ICME '23), vol. 126, pp. 561–566, Jan. 2024, ISSN: 2212-8271. DOI: 10.1016/j.procir.2024.08.240. [Online]. Available: https://www.sciencedirect.com/science/article/pii/S2212827124008072.

[14] D. Rauner, N. Eilers, H. Panzer, L. Frei, and M. F. Zaeh, "Prediction of shrink lines in powder bed fusion of metals using a laser beam by means of a finite element simulation approach," *Journal of Advanced Joining Processes*, vol. 11, p. 100 315, Jun. 2025, ISSN: 2666-3309. DOI: 10.1016/j.jajp.2025.100315. [Online]. Available: https://www.sciencedirect.com/science/article/pii/S2666330925000366.

[15] I. Setien, M. Chiumenti, M. San Sebastian, M. A. Caicedo, and C. A. Moreira, "Defining and Optimising High-Fidelity Models for Accurate Inherent Strain Calculation in Laser Powder Bed Fusion," en, *Metals*, vol. 15, no. 2, p. 180, Feb. 2025, ISSN: 2075-4701. DOI: 10.3390/met15020180. [Online]. Available: https://www.mdpi.com/2075-4701/15/2/180.

[16] E. Neiva, M. Chiumenti, M. Cervera, E. Salsi, G. Piscopo, S. Badia, A. F. Martín, Z. Chen, C. Lee, and C. Davies, "Numerical modelling of heat transfer and experimental validation in powder-bed fusion with the virtual domain approximation," *Finite Elements in Analysis and Design*, vol. 168, p. 103 343, 2020, ISSN: 0168-874X. DOI: https://doi.org/10.1016/j.finel.2019.103343. [Online]. Available: https://www.sciencedirect.com/science/article/pii/S0168874X19302070.

[17] J. Baiges, M. Chiumenti, C. A. Moreira, M. Cervera, and R. Codina, "An adaptive finite element strategy for the numerical simulation of additive manufacturing processes," en, *Additive Manufacturing*, vol. 37, p. 101 650, Jan. 2021, ISSN: 2214-8604. DOI: 10.1016/j.addma.2020.101650.

[18] C. A. Moreira, M. A. Caicedo, M. Cervera, M. Chiumenti, and J. Baiges, "An accurate, adaptive and scalable parallel finite element framework for the part-scale thermo-mechanical analysis in metal additive manufacturing processes," en, *Computational Mechanics*, vol. 73, no. 5, pp. 983–1011, May 2024, ISSN: 1432-0924. DOI: 10.1007/s00466-023-02397-6. Accessed: Dec. 20, 2024. [Online]. Available: https://doi.org/10.1007/s00466-023-02397-6.

[19] I. Setien, M. Chiumenti, M. San Sebastian, C. A. Moreira, and M. A. Caicedo, "Integrating temperature history into inherent strain methodology for improved distortion prediction in laser powder bed fusion," *Metals*, vol. 15, no. 2, 2025, ISSN: 2075-4701. DOI: 10.3390/met15020143. [Online]. Available: https://www.mdpi.com/2075-4701/15/2/143.